ROYAL SOCIETY
OF CHEMISTRY

PAPER

Understanding the efficiency drooping of the deep blue organometallic phosphors: a computational study of radiative and non-radiative decay rates for triplets†

Qian Peng,[a] Qinghua Shi,[a] Yingli Niu,[a] Yuanping Yi,*[a] Shaorui Sun,[c] Wenqiang Li[b] and Zhigang Shuai*[b]

High-efficiency deep blue organometallic phosphors are imperative to organic luminescence devices. While green iridium complexes commonly exhibit high luminescence efficiencies, the luminescence quantum efficiency always drops sharply when emission becomes deep blue. In this work, the microscopic mechanism of such a drastic decrease is elucidated from detailed computational investigation. Both radiative (k_r) and non-radiative (k_{nr}) decay rates of the lowest triplet state (T_1) are calculated for five representative cyclometalated iridium(III) complexes with emission color ranging from green to deep blue, based on phenylpyridyl, phenylpyrazolyl, bipyridinato, pyrimidinpyridyl, and pyrimidinprazolyl ligands. For all compounds, the T_1 states are characteristic of mixed intraligand ($\pi \rightarrow \pi^*$) transition and iridium-to-ligand charge transfer (d $\rightarrow \pi^*$), and the increased $\pi \rightarrow \pi^*$ and decreased d $\rightarrow \pi^*$ portions lead to the blue-shifted emission of **1** < **2** < **4** < **5** < **3**. Strikingly, it is found that the drastic increase of k_{nr} arising from severe intra-ligand vibration relaxations induced by the enhanced $\pi \rightarrow \pi^*$ transition is mainly responsible for the droop of the phosphorescence quantum efficiency, which provides a different deactivation mechanism from the thermally-activated transformation into a dark metal-centred ligand field excited state reported in many previous studies. Compared with the well-studied compounds **1–3**, the newly designed compounds **4** and **5** achieve a good balance between high efficiency and a large energy gap and are very promising as deep blue phosphors. These findings are expected to be helpful for the rational design of high-efficiency blue organometallic phosphors, especially in terms of ligands.

[a] *Beijing National Laboratory for Molecular Sciences (BNLMS), CAS Key Laboratory of Organic Solids, Institute of Chemistry, Chinese Academy of Sciences, Beijing 100190, China. E-mail: ypyi@iccas.ac.cn*

[b] *Key Laboratory of Organic Optoelectronics and Molecular Engineering, Department of Chemistry, Tsinghua University, Beijing 100084, China. E-mail: zgshuai@tsinghua.edu.cn*

[c] *College of Environmental and Energy Engineering, Beijing University of Technology, Beijing 100124, China*

† Electronic supplementary information: Tests of basis sets and solvent effects, molecular orbital composition of FMOs and the coefficients of the main transitions as well as the adiabatic excitation energies of the emissive triplet state at the ground-state optimized geometries for **1–5**, the properties of the six lowest excited singlet states of **1–5**; the displacement vectors of the vibration normal modes involved in the emission spectra, calculated spin–orbit coupling matrix elements between T_1 and S_0 for **1–5**, the derivation of the approximate intersystem crossing rate formula eqn (2), reorganization energies and Huang–Rhys factors *versus* the normal mode wavenumbers for **1–5**, selected reorganization energy and the corresponding vibrational normal mode frequencies of **1–5**, and the selected structure parameters in the S_0 and T_1 states and the corresponding modification between the two states for **1–5**. This material is available from the Wiley Online Library or from the author. See DOI: 10.1039/c6tc00858e

1. Introduction

Organic light-emitting diodes (OLEDs) have been the focus of considerable academic and industrial research due to their potential applications in the highly efficient soft large-area display and color-rendering solid state lighting.[1–4] Owing to harvesting emission from both singlet and triplet states, a vast amount of phosphors, with emission ranging from near-UV to near-infrared, has been extensively developed.[5] Recent progresses in green and deep blue phosphorescent OLEDs are very exciting.[6] However, achieving highly efficient and stable deep blue phosphorescence is still very challenging.[7] Cyclometalated iridium complexes are the most preferred phosphors for OLEDs and have been extensively synthesized; their emission colors can be arbitrarily tuned in the full color range by changing the chemical ligands.[5,8–12] Even so, it is a grand challenge to obtain highly efficient deep blue iridium complexes since the luminescence quantum efficiency (LQE) drops drastically when the emission becomes deep blue.[13–19] Through characterizing the photophysical properties of a series of iridium complexes,

the decline of LQE is ascribed to a significant decrease in the radiative rates caused by increased energy separation between the metal-ligand charge transfer (MLCT) singlet and the ligand-centered triplet states.[13] By using time-resolved photoluminescence measurements, the increase in the non-radiative decay rate is found to be responsible for the droop of the LQE.[14] It was claimed that the emissive T_1 is thermally activated to transform into a dark metal-centered (MC) excited triplet ^3MC state, and then nonradiatively decays to the ground state (S_0) via $S_0/^3MC$ crossing.[20,21] In this work, we have explored the efficiency drooping mechanism of deep blue organometallic phosphors, and have established the relationship between the molecular structure and the photophysical properties through quantitative calculations of the vibrationally resolved emission spectra, and radiative and nonradiative rate constants, providing helpful insights into the rational design of high-efficiency phosphorescent materials based on organometallic compounds.

Based on the fundamental first-order perturbation rate theory,[22] the radiative rate constant is directly proportional to the spin–orbit coupling (SOC) between the emitting states and the perturbing intermediate states with different multiplicities, and the electric transition dipole moment between the involved electronic states with the same multiplicity, but it is inversely proportional to the energy gap between the interacting triplet and singlet excited states. The non-radiative decay rate constant between the triplet and singlet states depends on the SOC, energy gap and vibronic coupling. For many organic fluorescent compounds, vibronic couplings have been found to play an indispensable role in determining the non-radiative decay rates.[23] It is highly desirable to find which factor is the most important one to determine the radiative or non-radiative rate constants and to provide good ideas for the molecular design of highly efficient blue iridium(III) complexes.

Here, we have chosen five representative facial (fac) cyclometalated iridium(III) complexes based on bare and fluorine-substituted phenylpyridyl (ppy), phenylpyrazolyl (ppz), bipyridinato (pypy), pyrimidinpyridyl (pmpy), pyrimidinprazolyl (pmpz) ligands (see Chart 1), and quantitatively computed their radiative and non-radiative rate constants and vibrationally resolved emission spectra by using the thermal vibration correlation function (TVCF) rate theory in combination with the DFT/TDDFT calculations.[20] And the key factors that control the emission energy and the radiative and non-radiative rate constants have been carefully elucidated.

2. Computational details

The geometry optimizations and vibrational frequency calculations for the S_0 and T_1 states of all the studied compounds were respectively performed by using the restricted closed-shell density functional theory (DFT) and unrestricted DFT with the B3LYP hybrid functional, which was successfully applied for the calculations of various iridium(III) compounds.[24,25] Based on the optimized geometries and vibrational normal modes, the reorganization energies and vibronic coupling coefficients were calculated reliably (see the computational methods in the ESI†). The long-range separated hybrid functional CAM-B3LYP was then used to compute the adiabatic energy difference between the S_0 and T_1 states through considering the long-range interaction. These geometric and electronic structure calculations were conducted using the Gaussian 09 program.[26] Based on the ground-state geometries, the spin–orbit coupling matrix elements and transition dipole moments between singlet and triplet states were respectively evaluated using the linear and quadratic response theories in the framework of TDDFT with the B3LYP functional, as implemented in the Dalton program.[27] The influence of different basis sets on the optimized geometries, spin–orbit coupling matrix elements and transition dipole moments was discussed in Section I of the ESI† (Tables S1–S3). The basis set combining Stuttgart Dresden ECP (SDD) for heavy atom Ir(III) and 6-31G** for light atoms is turned out to excellently balance computational costs and good accuracies and was adopted throughout all the calculations. In addition, the solvent effect on the geometrical structure relaxations of S_0 and T_1 states was tested for compound **1** by using the common polarizable continuum model,[28] respectively, and it is found to be insensitive to the solvent environments (see Section III of the ESI†).

The potential energy surfaces of two electronic states T_1 and S_0 could be different if considering the torsion and Duschinsky rotation effects, in addition to the origin displacement. Herein, the displacement vector was respectively computed by $D_{T1} = L_{T1}^T \Delta x$ and $D_{S0} = L_{S0}^T \Delta x$, in which L_{T1}/L_{S0} are the eigenvector matrix of the mass weighted force constants of T_1/S_0 states and Δx is the difference between the molecular Cartesian coordinates at the equilibrium positions of the two electronic states. The Duschinsky rotation matrices were calculated by $S = L_i^T L_f$. Finally, based on all the geometric and electronic structure information obtained above, the phosphorescence spectra and the radiative and non-radiative rate constants were evaluated by using the multimode coupled spectrum and rate theories,
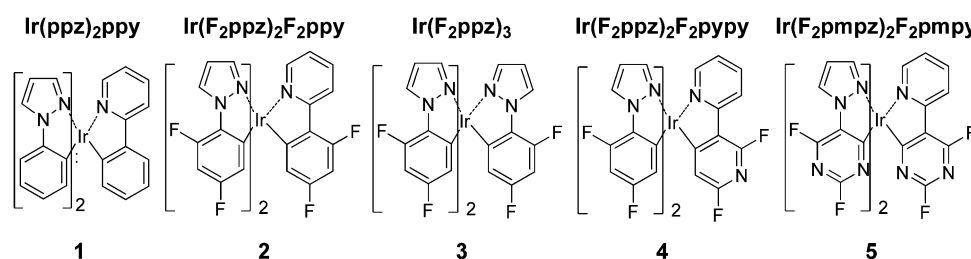

Chart 1 Molecular Structures of compounds **1–5**.

which are provided in detail in the ESI† and our previous work.[20,29] All these calculations were carried out using the home-built MOMAP program.[30]

3. Results and discussion

3.1. Electronic transition properties

To shed light on the origin of different emission wavelengths or colors of the cyclometalated iridium complexes, we have analyzed the nature of the T$_1$ state. First, the frontier molecular orbitals (FMOs) of the ligands are examined and plotted in Fig. 1. It can be easily seen that both the HOMO and the LUMO are delocalized over the whole molecules owing to the strong molecular conjugation. Compared with the ppy-like series, the FMO energy levels of the ppz-like series are raised, especially for the LUMO, which leads to relatively larger HOMO–LUMO gaps. Upon substitution of ppy and ppz with electron-withdrawing fluorine atoms, the FMO levels are stabilized and a bit more for the LUMO, which results in a slight decrease in the HOMO–LUMO gap for F$_2$ppy and F$_2$ppz. Incorporation of nitrogen atoms in the phenyl rings of F$_2$ppy and F$_2$ppz further brings down the HOMO and LUMO levels to an even greater extent. For the ppy-like series, the severe decrease for the HOMO results in a larger HOMO–LUMO gap. On the contrary, the sharper decrease for the LUMO causes a smaller energy gap in the ppz-like series. Consequently, F$_2$pmpy and F$_2$pmpz exhibit similar and relatively large energy gaps as well as deep HOMO levels, which is important for stable blue emission.

The energy levels of selected FMOs of compounds **1–5** are shown in Fig. 2 as well as the important transitions of the T$_1$ state, and their compositions and profiles are respectively presented in Table S6 and Fig. S1 (ESI†). The FMOs of the compounds are constituted by the FMOs of the ligands and the
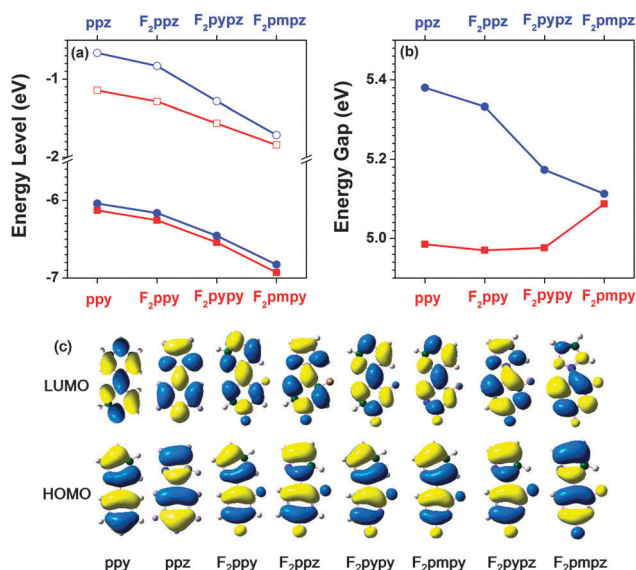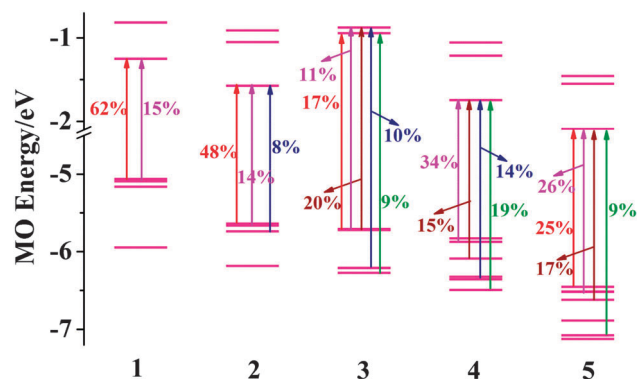

Fig. 2 The energy levels of the selected frontier molecular orbitals and the important transitions for the emissive T$_1$ at the optimized ground-state geometries for **1–5**.

d-orbitals of the iridium atom. In the case of an octahedral symmetry, the d-orbitals of the iridium atom are split into two subsets, three t$_{2g}$ (d$_{xy}$, d$_{xz}$, d$_{yz}$) orbitals and two e$_g$ (d$_{x^2-y^2}$, d$_{z^2}$) orbitals. Generally, the three degenerate occupied t$_{2g}$ orbitals of iridium are hybridized with the π orbitals of three ligands to constitute the six highest occupied FMOs of the complex. As seen from Table S5 (ESI†), for all the complexes, the HOMO, HOMO−1, and HOMO−2 consist of ∼40% component from the iridium d-orbitals and ∼60% component from the ligand π-orbitals. In the case of **3**, the HOMO is delocalized quite evenly over the three same ligands (see Fig. S1, ESI†) and very close to the degenerate HOMO−1 and HOMO−2 in energy (see Fig. 2 and Table S5, ESI†). For the other complexes, possessing two different kinds of ligands, the energy difference between the HOMO, HOMO−1 and HOMO−2 becomes larger, especially between HOMO−1 and HOMO−2. Interestingly, although the ligands have close or the same HOMO energies, the d-orbital composition is reduced with the decrease in energy from the HOMO through HOMO−1 to HOMO−2 in the complexes except for **4**. In addition, for all the complexes, HOMO−3 holds a small d-orbital component and its energy is remarkably lower than that of HOMO−2. As expected, the HOMO is stabilized by substitution with fluorine atoms (**1** → **2**, **3**, and **4**). Moreover, much bigger stabilization upon fluorination is found for the complex with respect to the isolated ligands due to larger distribution of the HOMO on the phenyl ring that is connected with iridium by a σ bond. Upon the introduction of one nitrogen atom in the phenyl ring of the pypy ligand, the HOMO energy of **4** becomes much lower with respect to **2** and **3**. Incorporation of two nitrogen atoms in the phenyl ring of each ligand results in an extremely low HOMO energy for **5**.

Since the unoccupied e$_g$ d*-orbitals of iridium are lying much higher above the LUMOs of ligands,[31] d*–π* hybridization is effectively prevented. Furthermore, owing to a much lower LUMO energy for the ppy-like ligand than the ppz-like ligand, the complex LUMO for **1–5** is dominated by the LUMO of ppy, F$_2$ppy, F$_2$ppz, F$_2$pypy, and F$_2$pmpy, respectively. Thus, following the energy order of the ligand LUMOs in Fig. 1, the LUMO energies for the complexes are decreased in the order of

Fig. 1 The energy levels of the HOMO (a), energy gap between HOMO and LUMO (b), and the charge density contours of HOMO and LUMO at the optimized ground-state geometries for the ligands (c).

This journal is © The Royal Society of Chemistry 2016

J. Mater. Chem. C, 2016, **4**, 6829–6838 | **6831**

Table 1 Calculated non-adiabatic excitation energies, radiative and non-radiative rate constants and the maximum emissive peaks at 298 K for compounds **1–5**, as well as the available experimental values in parentheses

|	ΔE_{ad}/eV	λ_{max}/nm, 298 K	k_r/s^{-1}	k_{nr}/s^{-1}
1	2.81	496.1 (500)[a]	1.47×10^5 $(4.2$–$5.6 \times 10^5)^{a,b}$	3.08×10^5 $(0.29$–$2.0 \times 10^5)^{a,b}$
2	2.99	467.0 (457)[a]	1.14×10^5 $(4.6 \times 10^5)^a$	2.47×10^5 $(3.1 \times 10^5)^a$
3	3.40	435.8	1.70×10^4	3.43×10^7 $(\sim 10^8)^a$
4	3.09	453.8	1.04×10^5	2.35×10^6
5	3.12	447.9	4.26×10^4	3.97×10^6

[a] Ref. 18. [b] Ref. 33.

3 > **1** > **2** > **4** > **5** in Fig. 2. In the case of **3**, because all the ligands are F$_2$ppz, the LUMO+1 and LUMO+2 also stem from the F$_2$ppz LUMO, and their energy levels are degenerate and close to the LUMO. However, LUMO+1 for the other four complexes stem from either LUMO+1 of the same ppy-like ligands or the LUMO of the other ppz-like ligands and are thus significantly (>0.5 eV) higher relative to the complex LUMO. Similar to the isolated ligands, the complex LUMO is delocalized over the py or pz ring linking to iridium by a coordinate bond; hence, replacement of the heterocyclic py with pz can result in a dramatic increase in the LUMO energy for **3** with respect to the other four compounds. Compared with the HOMO, the decrease in the LUMO energy is relatively smaller upon fluorination or nitrogenization. As a result, the HOMO–LUMO gap is increased in the order of **1** < **2** ≈ **4** < **5** < **3**.

As seen from Fig. 2, the T$_1$ state of **1** mainly stems from the transition from the quasi-degenerate HOMO and HOMO−1 to the LUMO. Compared with **1**, more excitations from the deeper occupied orbitals to the LUMO contribute to the T$_1$ state for the other compounds, in particular for **4**. Consequently, the T$_1$ energy is increased in the order of **1** < **2** < **4** < **5** < **3** (see Table 1). In order to characterize the nature of the S$_0$ → T$_1$ transition for the complexes, natural transition orbital (NTO) analysis was carried out at the optimized ground-state geometries. The hole and electron NTOs and their proportions are shown in Fig. 3. Clearly, for **1**, **2**, **4**, and **5**, the hole and the electron are mainly concentrated on the single ppy-like ligand rather than the other two ppz-like ligands, while extend to all the three F$_2$ppz ligands for **3**. The hole and electron NTOs are dominated by the relevant ligand HOMO and LUMO, respectively. Owing to the lack of considerable exchange energy, the inter-ligand transition is negligible. In addition, for all the compounds, the hole NTO includes an important ingredient from the metal iridium. Relatively, the metal ingredient is much smaller for the electron NTO. Thus, the T$_1$ state of **1–5** exhibits a mixed (major) intra-ligand and (minor) metal-ligand charge transfer character, which has been found in many iridium complexes reported previously.[14,32] As seen from Fig. 2, it is very clear that the enhancement of excitation energy of T$_1$ is caused by the transitions involving more inner or outer molecular orbitals for **1** → **2** → **4**.

3.2. Emission spectra and luminescence quantum efficiencies

The emission spectra are very helpful to get deep insight into the photophysical properties. In particular, the vibrationally resolved spectra at low temperatures can be used to elucidate the electronic transition properties and electron-phonon interaction.
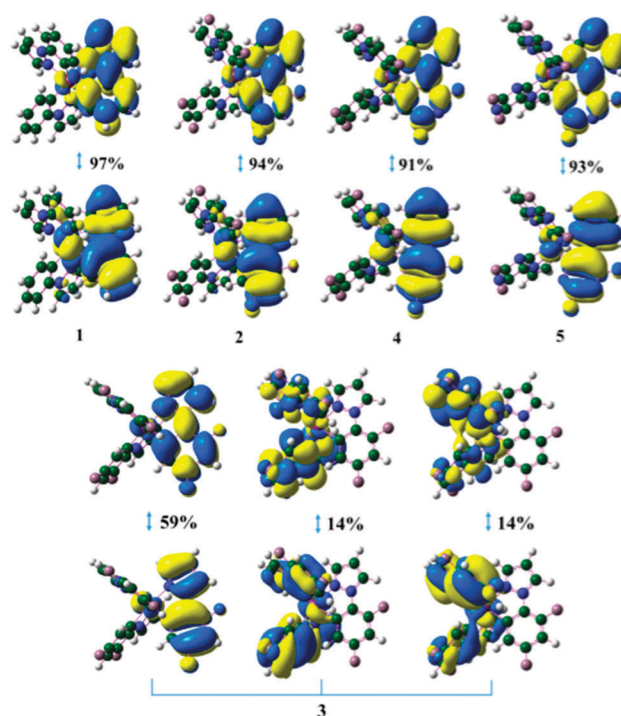
Fig. 3 The hole (bottom) and electron (top) pairs and the corresponding proportions for the S$_0$ → T$_1$ transition obtained by natural transition orbital analysis at the optimized ground-state geometries for **1–5**.

Therefore, the spectra at various finite temperatures have been evaluated by assuming the three triplet substrates to be equally populated due to the fast spin relaxation. This assumption seems to be reasonable because the fine-structure feature caused by the difference among the three electronic substrates is generally observed below 25 K in organometallic complexes.[9] It should be noted that the spectra at finite temperatures can be naturally broadened using the thermal vibration correlation function method without any artificial Gaussian or Lorentzian broadening. The calculated and experimental spectra at 77 K for **3** are shown in Fig. S2 (ESI†), which match well with each other even in the spectral fine-structure features. This confirms that the current quantum chemistry method and spectrum theory are appropriate to describe the photophysical properties of the organometallic complexes. Fig. 4 shows the calculated spectra at 0, 77, 196 and 298 K for all the compounds **1–5**. Coinciding with the triplet energies, the emission spectra are blue-shifted in the order of **1** > **2** > **4** > **5** > **3** (see Table 1). Despite different shifts and intensities, the overall profiles are very similar for compounds **1**, **2**,

Fig. 4 The calculated emission spectra (a) at 0 K (the individual vertical spectral lines can be assigned to the involved vibrational states of the S_0 state, which are labeled as n^x with n the vibrational normal mode and x the vibrational quantum number) and (b) at finite temperatures for compounds **1–5**.

4, and **5**, while significantly varying from that for **3** due to the distinct type of ligands involved in the $T_1 \to S_0$ transition (the ppz-like ligands for **3** and the ppy-like ligands for the other compounds). For every compound, the spectrum exhibits fine structures at low temperatures, comprising of the purely 0–0 transition band and the vibrational satellites. The origin of the emission bands and the contribution of the vibration modes to such bands for compounds **1–5** can be fairly figured out from the spectra at 0 K as shown in Fig. 4a. The wavenumbers and displacement vectors of the involved normal modes are given in Fig. S3 (ESI†). For the compounds, the first significant band near 0–0 transition is mainly caused by single-mode excitations of the out-of-plane vibrations of the ligands with low frequencies less than 200 cm^{-1} and metal–ligand bond/internal-ligand vibrational motions with moderate frequencies in the range of 500–700 cm^{-1}. The second band stems from single-mode excitations of the stretching vibrations of C–C/C–N bonds with high frequencies of ∼1400–1600 cm^{-1}. The third and fourth bands mainly come from mixed excitations of two modes or double excitations of a single mode. Also, it can be obviously seen from Fig. 4b that the relative intensity of the band made up of stretching vibrations in ligands (the second band) versus the band formed by the metal–ligand bond/internal-ligand vibrational motions (the first band) is gradually enhanced in the order of **1 → 2 → 4 → 5 → 3**. This feature is fully consistent with the fact that the contributions from the d → π* transition decrease but those from π → π* increase for the $T_1 \to S_0$ transition in the same order among these compounds. In addition, the nature of the vibrational satellites completely corresponds to the distributions of the Huang–Rhys factors (see Fig. S4, ESI†), which are the key parameters to characterize vibronic couplings. As the temperature is increased, the fine structures of the spectra are gradually smeared out and become very smooth at room temperature. At the same time, the intensities of the 0–0 transition peak get weakened while the side vibrational bands become more dominant, leading to bathochromic shifts of the emission with increasing temperatures.

For an organometallic compound, the luminescence quantum efficiency depends on the competition between the radiative and non-radiative decay rates from T_1 to S_0. Table 1 lists the radiative and non-radiative rate constants and the maximum peaks of the emissive spectra as well as the available experimental values at 298 K for all the compounds **1–5**. The calculated results are in good agreement with the experimental data on the order of magnitude. Relative to **1**, both the radiative and non-radiative rate constants are slightly reduced for **2**, eventually leading to a little decrease of LQE while achieving a blue shift of 29 nm in the maximum emission peak. In spite of the remarkable hypsochromic shift of 60 nm for **3** versus **1**, the radiative rate constant falls by almost one order of magnitude and the non-radiative rate rises sharply even by two orders of magnitude, which results in an extremely low LQE. It appears that a fine trade-off between blue emitting color and high quantum efficiency can be achieved in compounds **4** and **5**. Compared with **3**, while the emission spectra of **4** and **5** are somewhat red-shifted, their quantum efficiencies turn out to be much higher due to the cooperative effect of large enhancement of radiative rates and reduction of non-radiative rates. This indicates that compounds **4** and **5** are good candidates for blue/deep blue phosphors with the maximum peaks at 454 nm and 448 nm at room temperature, respectively. Nevertheless, it would be highly desirable to understand the molecular factors regulating the radiative and non-radiative rates associated with the blue-shifted emission and how to boost the radiative rate while restraining the non-radiative rate through tuning chemical structures. In the following, the origins of the T_1 state decay and the factors governing the decay rates will be discussed in detail.

3.3. Radiative decay

The radiative decay rate constant k_r is calculated as the integration of the emission spectrum over the whole range. In the formalism for spectrum calculation, the electric transition dipole moment (μ), adiabatic excitation energy (ΔE_{ad}) and vibronic coupling are three fundamental physical parameters.[27,34] As pointed out by previous work, the vibronic couplings mainly determine the shape and width of an emission spectrum but hardly change the integration of the spectrum.[21] This can also be seen from the nature of emission spectra at different temperatures. Taking compound **1** as an example, the radiative decay rate constants are calculated to be 1.53×10^5 s^{-1} at 77 K, 1.50×10^5 s^{-1} at 196 K and 1.47×10^5 s^{-1} at 298 K, which are almost equivalent although the spectra vary considerably. Therefore, the radiative rates are primarily controlled by μ and ΔE_{ad}. Actually, the direct electric transition dipole between the triplet and singlet states is spin-forbidden. In the organometallic complexes, the heavy element effect of the metal atom brings about significant spin–orbit coupling between the singlet and triplet states, which results in perturbation of the emissive singlet with triplet states. Consequently, the admixed states can enable the optical transition from the triplet state to the ground state. Similarly, the ground state can also mix with intermediate triplet states through spin–orbit couplings. Thus, under the

This journal is © The Royal Society of Chemistry 2016

J. Mater. Chem. C, 2016, **4**, 6829–6838 | **6833**

first-order perturbation theory, the μ between T_1 and S_0 can be expressed as

$$
\mu_{S_0 \leftarrow T_{1,m}} \equiv \sum_{l \in \text{singlets}} \frac{\langle S_0 | \hat{\mu} | S_l \rangle \langle S_l | \hat{H}^{SO} | T_{1,m} \rangle}{E_{T_1} - E_{S_l}}
$$
$$
+ \sum_{n \in \text{triplets}} \sum_{j=-1,0,1} \frac{\langle S_0 | \hat{H}^{SO} | T_{n,j} \rangle \langle T_{n,j} | \hat{\mu} | T_{1,m} \rangle}{E_{S_0} - E_{T_n}}
$$

(1)

The second term is often negligible because the energy gaps between the ground state (S_0) and the triplet states are relatively very large. Therefore, $\mu_{S_0 \leftarrow T_{1,m}}$ is controlled by the following three factors: the SOC of T_1 with the intermediate excited singlet states (S_l), the electric transition dipole moment between S_0 and S_l, and the energy gaps between S_l and T_1.

To avoid the time-consuming issue to solve the complicated four-component Dirac equation, the SOC is calculated within the effective nuclear charge (Z_{eff}) approximation of the Breit–Pauli Hamiltonian. Since the scaled charge of iridium for spin–orbit integrals is 1150.38, much larger than those of other atoms, i.e., C (3.60), N (4.55), F (6.75) and H (1.00) in **1–5**, the SOC involving atoms other than iridium can be neglected. Therefore, an increase in the proportion of the iridium d-orbital in the electronic transition configuration of T_1 can remarkably strengthen the SOC. Since the T_1 shows strong metal–ligand charge transfer (MLCT) character, the intermediate S_l states with obvious MLCT nature will be effectively coupled to the T_1 state according to the symmetry selection rule. Fig. S5 (ESI†) shows the properties of the lowest ten singlet excited states and the T_1 state at the optimized ground-state geometries for **1–5**, including ΔE, μ, and the iridium d-orbital components of the transition configurations. As seen from Fig. S5 (ESI†), (i) the d-orbital proportion in the $S_0 \rightarrow T_1$ transition is decreased in the order of **1 > 4 ≈ 2 > 5 > 3**, with the respective values of 25%, 17%, 16%, 12% and 7%; (ii) for all the compounds, most of the singlet excited states have outstanding MLCT characteristics with similar d-orbital components more than 30%, indicating that these singlet excited states can well interact with the T_1 state and the relative interaction strengths among these compounds are mainly dependent on the MLCT nature of the emissive T_1 states; (iii) the largest transition dipole moment to the ground state occurs in the S_3 state for **1, 2, 4** and **5** in a descending order (1.78, 1.73, 1.50 and 1.27 Debye, respectively), but in the much higher S_7 and S_8 states in **3** (1.71 or 1.73 Debye). By and large, the transition dipole moments between the S_0 and T_1 states are obtained to decrease in the order of **1 > 2 > 4 > 5 > 3** with the values of 0.26, 0.21, 0.20, 0.13 and 0.07 Debye, respectively. Since the MLCT degree can play an important role in the determination of the electric transition dipole moment and the T_1 excitation energy, it would be interesting to compare the relationship between the radiative rate constant and the iridium d-orbital proportion of the T_1 state. As seen from Fig. 5, a strong positive correlation is revealed between the radiative decay rate constants and the differences in the iridium d-orbital component between hole and electron NTOs for the $S_0 \rightarrow T_1$ transition. This suggests that it is important to tune the metal proportion in the transition configuration of the lowest triplet state
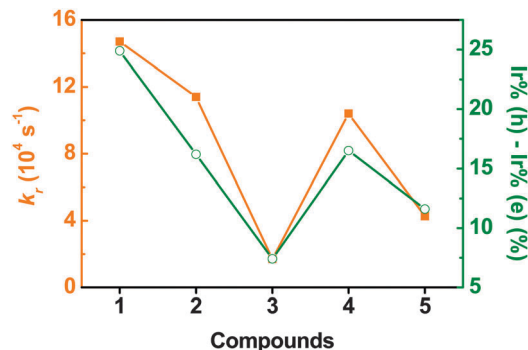

Fig. 5 Plots of the radiative decay rate constants (full squares) and the differences in the iridium d-orbital component in percent between hole and electron obtained by natural transition orbital analysis (open circles) for **1–5**.

in order to obtain a high radiative decay rate in the design of new organometallic complexes.

3.4. Non-radiative decay

For the five compounds, the spin–orbit coupling elements (>100 cm^{-1}) are much larger than those in pure organic fluorescent molecules (<1.0 cm^{-1}).[20] Therefore, it is reasonable to calculate the non-radiative rate constant (k_{nr}) by using the first-order perturbation rate formula.[20] In order to intuitively analyze the non-radiative rate constant, the formula is simplified by applying the short-time approximation under the framework of the displaced harmonic oscillator model (see more details in the ESI†),

$$
\ln[k_{nr}(T_1 \rightarrow S_0)] = -\frac{\left(\Delta E_{ad} - \sum_k \lambda_k\right)^2}{4 \sum_k \lambda_k \bar{E}_k}
$$
$$
+ \ln\left(\frac{1}{\hbar} |\langle S_0 | \hat{H}^{SO} | T_1 \rangle|^2 \sqrt{\frac{\pi}{\sum_k \lambda_k \bar{E}_k}}\right)
$$

(2)

where ΔE_{ad} denotes the adiabatic excitation energy; $\lambda_k = S_k \hbar \omega_k = \omega_k^2 D_k^2 / 2$ is the reorganization energy for the kth mode; S_k and D_k are the Huang–Rhys factor and displacement of the corresponding mode with frequency ω_k, respectively; $\bar{E}_k = (\bar{n}_k + 1/2)\hbar \omega_k$ is the average vibration energy and $\bar{n}_k = (\exp(\hbar \omega_k / k_B T) - 1)^{-1}$ the phonon occupation number; $\hbar$, k_B, and T represent Planck's constant, the Boltzmann constant and temperature, respectively. As seen from eqn (2), adiabatic excitation energy, reorganization energy and spin–orbit coupling between T_1 and S_0 are three key parameters to govern the non-radiative rate constant. According to eqn (2), as a whole, the plot of $\ln(k_{nr})$ versus ΔE_{ad} is a downward parabola with the symmetric axis of $\Delta E_{ad} = \sum_k \lambda_k$ and the latus rectum of $4 \sum_k \lambda_k \bar{E}_k$. The evolution of k_{nr} as a function of ΔE, i.e. the so-called non-radiative rate constant spectrum, is shown in Fig. 6a; it gives the rate constant $k_{nr} = k_{nr}(\Delta E_{ad})$ if $\Delta E = \Delta E_{ad}$. For the studied compounds, since the ΔE_{ad} of 2.82–3.12 eV are much

6834 | J. Mater. Chem. C, 2016, **4**, 6829–6838
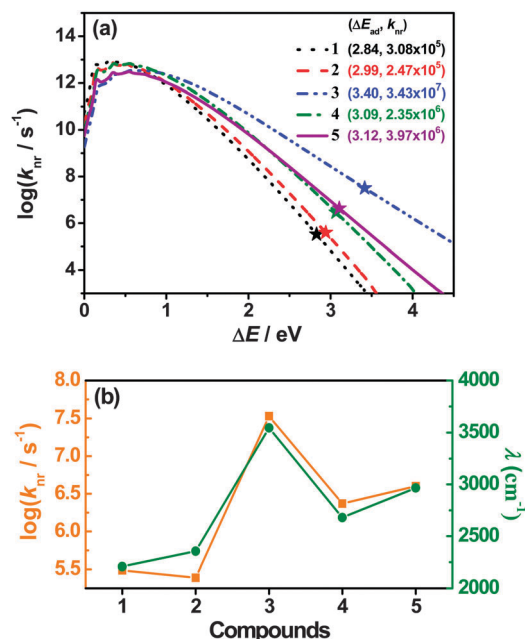
This journal is © The Royal Society of Chemistry 2016

Fig. 6 (a) Non-radiative decay rate constant spectra for **1** (black dot), **2** (red dash), **3** (blue dash dot dot), **4** (green dash dot), and **5** (purple solid) at 298 K, and the real values of $\log(k_{nr})$ are located at $\Delta E = \Delta E_{ad}$ (marked by pentastars); (b) plots of the non-radiative decay rate constants (squares) and the total reorganization energies on the potential energy surfaces of the T_1 state (circles) for **1–5**.

larger than the corresponding λ of 0.25–0.44 eV, the respective rates fall into the inverted Marcus region and the k_{nr} value decreases with the increase of ΔE. Moreover, when ΔE is large enough, the value of $\ln(k_{nr})$ decreases approximately linearly with ΔE. The phenomenon is consistent with the energy gap law for non-radiative transitions in the weak coupling limit,[33,35–38] although the total Huang–Rhys factors are quite strong with the values of 3.12, 2.68, 3.87, 3.24, and 4.13 for **1–5**, respectively. It should be noted that the non-radiative rate constant spectrum curves exhibit varied vertices and widths for the different complexes. In fact, larger ΔE_{ad} leads to a faster non-radiative decay in all the studied compounds except for **1** and **2**. Thus it would be unreasonable to compare the non-radiative rates between different compounds based solely on the energy gap law.

As presented in Table 2, the calculated SOCs of the T_1 state decrease in the order of **1** > **4** > **2** > **3** > **5**, which is inconsistent and even in contrast with the order for k_{nr}. On the other hand, the non-radiative decay rate is proportional to

the square of the spin–orbit coupling elements; this can lead to modulation of k_{nr} by at most 2.3 times; however, the real change in the five compounds exceeds two orders of magnitude. Therefore, the excitation energy and spin–orbit coupling do not appear to be responsible for the increase in the non-radiative decay with a blue shift. Since the total reorganization energy $\lambda = \sum_k \lambda_k$ approximately controls the width of the k_{nr} spectrum, it would play a decisive role in determining k_{nr}. Indeed, a strong correlation is found between the non-radiative decay rate constant and the total reorganization energy obtained from the potential energy surface of the excited state (see Fig. 6b). Compounds **1** and **2**, featuring the smallest reorganization energies, exhibit the lowest values of k_{nr}. As the reorganization energy increases, the non-radiative rate is continuously enhanced for compounds **4**, **5**, and **3**. This result suggests that the control of reorganization energies can really regulate the non-radiative decay rates for the complexes. It is not too surprising because the excess energy of the electronic excited state is converted into the molecular thermal vibrations in the non-radiative decay process and the magnitude of the reorganization energy represents the ability of vibrational normal modes to accept the excited-state energy. Therefore, it is important to understand how to modulate reorganization energies by modifying chemical structures for designing high-efficiency phosphors.

The reorganization energy of each vibrational normal mode (λ_k) for **1–5** is obtained and shown in Fig. S6 (ESI†). The corresponding data are collected in Table S5 (ESI†). The vibrational normal modes with large λ_k are regarded as important channels to non-radiatively dissipate the excited-state energies. For all the compounds **1–5**, the vibration normal modes with large reorganization energies appear in the range of ~ 1500–1680 cm^{-1}, corresponding to the stretching vibrations of C–C or C–N bonds. In order to gain an intuitive relationship between the property and the chemical structure, the reorganization energy is decomposed into the internal coordinates according to an approach we proposed previously.[39] The internal coordinates with the largest contributions are displayed in Fig. 7. Similarly, it is found that the main contributions to the reorganization energy come from the bonds instead of angles or dihedrals for all the compounds. In addition, the C–C and C–N bonds within the chromophore ligand can cause very large reorganization energies. Relatively, the stretching vibrations of the Ir–C and Ir–N bonds cost very small reorganization energies, less than 133 cm^{-1}. These results are further confirmed by the geometry modifications between the T_1 and S_0 states (see Tables S7–S11, ESI†). The largest contributions to the reorganization energy arise from the bonds, which form a five-membered ring in combination with iridium, *i.e.* the bonds between atoms **2**, **3**, **4**, and **5**. For instance, the C3–C4 bond vibrations cost the reorganization energies of 433, 503, 559, and 637 cm^{-1} for **1**, **2**, **4** and **5** respectively. In the case of **3**, the contribution to the reorganization energy from the N3–C4 bond vibration is even much larger, up to 998 cm^{-1}. To conclude, the bond vibration relaxations within the chromophore ligands dominate the non-radiative decay.

Table 2 Calculated spin–orbit coupling matrix elements (cm^{-1}) between T_1 and S_0 for compounds **1–5**

	1	2	3	4	5
$\langle S_0 \vert \hat{H}^{SO} \vert T_{1,x} \rangle$	97.35	95.54	−1.29	75.61	69.38
$\langle S_0 \vert \hat{H}^{SO} \vert T_{1,y} \rangle$	−262.81	−249.25	7.02	−288.38	−180.16
$\langle S_0 \vert \hat{H}^{SO} \vert T_{1,z} \rangle$	−118.56	−85.60	−242.21	−26.07	−65.58
Ave.[a]	175.69	161.84	139.90	172.78	117.72

[a] Ave. $= \sqrt{\left(\left| \langle S_0 \vert \hat{H}^{SO} \vert T_{1,x} \rangle \right|^2 + \left| \langle S_0 \vert \hat{H}^{SO} \vert T_{1,y} \rangle \right|^2 + \left| \langle S_0 \vert \hat{H}^{SO} \vert T_{1,z} \rangle \right|^2 \right) / 3}$.

This journal is © The Royal Society of Chemistry 2016

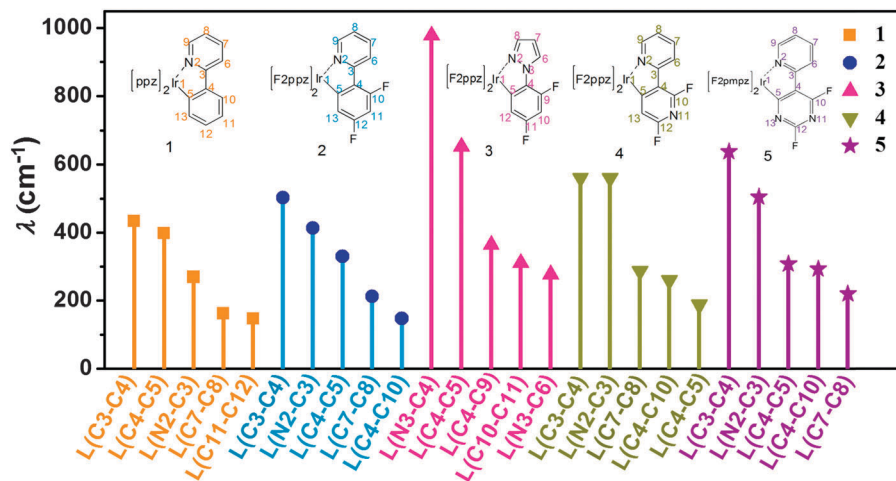*J. Mater. Chem. C*, 2016, **4**, 6829–6838 | 6835

Fig. 7 Selected internal coordinates with large reorganization energies for 1 (solid square), 2 (solid circle), 3 (solid uptriangle), 4 (solid downtriangle) and 5 (solid star) along with the relevant atomic labels shown in the inserts.

4. Conclusions

By means of thermal vibration correlation function rate theory coupled to DFT/TDDFT calculations, we have investigated the vibrationally resolved emission spectra, and the radiative and non-radiative decay processes of phosphorescent organometallic iridium(III) complexes with emission colors ranging from green to deep blue based on the bare and fluorinated ppy, pypy, ppz, pmpy and pmpz ligands. The calculated vibrationally resolved spectra and radiative and nonradiative decay rates are in good agreement with the available experimental data for compounds 1–3, and the drooping of luminescence quantum efficiency is well explained and understood at the molecular level. The TDDFT calculations reveal that the excitation energy of the T_1 state can be effectively elevated through fluorine substitutions and/or incorporation of nitrogen. All the complexes exhibit a mixed $d \rightarrow \pi^*$ MLCT and $\pi \rightarrow \pi^*$ IL character. The $d \rightarrow \pi^*$ components gradually decrease and the $\pi \rightarrow \pi^*$ ones correspondingly increase in the order of 1, 2, 4, 5 and 3 as the emission wavelength is blue shifted, which is further confirmed by the nature of the emission spectra. It is found that there is a strong positive correlation between the radiative decay rate constants and the differences in the iridium d-orbital component between hole and electron NTOs for the $S_0 \rightarrow T_1$ transition. The radiative decay is continuously dropped with the decrease in the metallic character in the emissive triplet state and in the order of 1, 2, 4, 5 and 3. The radiative decay rate constant of 3 is the lowest among the five compounds due to the smallest metal component in the emissive state. On the other hand, the non-radiative decay rate constant is mainly controlled by intramolecular reorganization energy. Due to the increase in molecular reorganization energy, the non-radiative decay rate constants are sharply boosted in the order of 1, 2 < 4 < 5 < 3, which is contrary to the energy gap law. The dramatically large reorganization energy of 3 leads to an extremely high non-radiative decay rate that is two orders of magnitude larger than those of 1 and 2. Because of the slight deceleration of radiative decay and severe acceleration of nonradiative decay, the luminescence quantum efficiency droops as the emission is blue-shifted, providing a different perspective from which nonradiative deactivation occurs via a thermally activated nonemissive metal-centered ligand state. The results of projecting the molecular reorganization energy into the internal coordinates (i.e. bond lengths and angles) point to the fact that the variation of the bond lengths within the chromophore ligands dominates the reorganization energy and specifically, the ppz-based ligands cost much larger reorganization energies with respect to the ppy-based ligand. Since a relatively large metal proportion exists in the transition configuration of the T_1 state and small intramolecular reorganization, the newly designed compounds 4 and 5, $Ir(F_2ppz)_2F_2pypy$ and $Ir(F_2pmpz)_2F_2pmpy$, are promising to be stable and efficient blue/deep blue phosphors. Our work would provide good ideas for the design and development of new high-efficiency blue or deep blue phosphors based on organometallic compounds.

In the present study, we only calculated the photophysical properties of the organometallic complexes in the gas phase or solution. As a matter of fact, the OLED devices are always operated in the solid state. Thus, it is necessary to consider the intermolecular electrostatic interaction, excitonic interaction and the polarization effect[40] for the solid-state organometallic complexes, which are being actively pursued.[41]

Acknowledgements

References

1 (a) S. Reineke, *Nat. Mater.*, 2015, **14**, 459; (b) X. L. Yang, G. J. Zhou and W. Y. Wong, *Chem. Soc. Rev.*, 2015, **44**, 8484; (c) S. Scholz, D. Kondakov, B. Lüssem and K. Leo, *Chem. Rev.*, 2015, **115**, 8449; (d) S. Hirata, Y. Sakai, K. Masui, H. Tanaka, S. Y. Lee, H. Nomura, N. Nakamura, M. Yasumatsu, H. Nakanotani, Q. Zhang, K. Shizu, H. Miyazaki and C. Adachi, *Nat. Mater.*, 2015, **14**, 330.

2 (a) Q. Zhang, B. Li, S. Huang, H. Nomura, H. Tanaka and C. Adachi, *Nat. Photonics*, 2014, **8**, 326; (b) K. Udagawa, H. Sasabe, C. Cai and J. J. Kido, *Adv. Mater.*, 2014, **26**, 5062; (c) T.-H. Han, Y. Lee, M.-R. Choil, S.-H. Wool, S.-H. Bae and B. H. Hong, *Nat. Photonics*, 2012, **6**, 105.

3 (a) S. Reineke, F. Lindner, G. Schwartz, N. Seidler, K. Walzer, B. Lussem and K. Leo, *Nature*, 2009, **459**, 234; (b) M. A. Baldo, D. F. O'Brien, Y. You, A. Shoustikov, S. Sibley, M. E. Thompson and S. R. Forrest, *Nature*, 1998, **395**, 151.

4 J. Kido, M. Kimura and K. Nagai, *Science*, 1995, **267**, 1332.

5 (a) H. Xu, R. F. Chen, Q. Sun, W. Y. Lai, Q. Q. Su, W. Huang and X. G. Liu, *Chem. Soc. Rev.*, 2014, **43**, 3259; (b) *Highly efficient OLED with phosphorescent Materials*, ed. H. Yersin, Wiley-VCH, Weinheim, 2008.

6 (a) M. G. Helander, Z. B. Wang, J. Qiu, M. T. Greiner, D. P. Puzzo, Z. W. Liu and Z. H. Lu, *Science*, 2011, **332**, 944; (b) J. Lee, H.-F. Chen, T. Batagoda, C. Coburn, P. I. Djurovich, M. K. Thomspon and S. R. Forrest, *Nat. Mater.*, 2015, **15**, 92.

7 L. X. Xiao, Z. J. Chen, B. Qu, J. X. Luo, S. Kong, Q. H. Gong and J. J. Kido, *Adv. Mater.*, 2011, **23**, 926.

8 A. B. Tamayo, B. D. Alleyne, P. I. Djurovich, S. Lamansky, I. Tsyba, N. N. Ho, R. Bau and M. E. Thompson, *J. Am. Chem. Soc.*, 2003, **125**, 7377.

9 H. Yersin, A. F. Rausch, R. Czerwieniec, T. Hofbeck and T. Fischer, *Coord. Chem. Rev.*, 2011, **255**, 2622.

10 Y. You and W. Nam, *Chem. Soc. Rev.*, 2012, **41**, 7061.

11 R. D. Costa, E. Ortí, H. J. Bolink, F. Monti, G. Accorsi and N. Armaroli, *Angew. Chem., Int. Ed.*, 2012, **51**, 8178.

12 C. L. Ho and W. Y. Wong, *Coord. Chem. Rev.*, 2013, **257**, 1614.

13 J. Li, P. I. Djurovich, B. D. Alleyne, M. Yousufuddin, N. N. Ho, J. C. Thomas, J. C. Peters, R. Bau and M. E. Thompson, *Inorg. Chem.*, 2005, **44**, 1713.

14 S. C. Lo, C. P. Shipley, R. N. Bera, R. E. Harding, A. R. Cowley, P. L. Burn and I. D. E. Samuel, *Chem. Mater.*, 2006, **18**, 5119.

15 C. S. K. Mak, A. Hayer, S. J. Pascu, S. F. Watkins, A. B. Holmes, A. Köhler and R. H. Friend, *Chem. Commun.*, 2005, 4708.

16 P. Coppo, E. A. Plummer and L. De Cola, *Chem. Commun.*, 2004, 1774.

17 T. Sajoto, P. I. Djurovich, A. B. Tamayo, M. Yousufuddin, R. Bau, M. E. Thompson, R. J. Holmes and S. R. Forrest, *Inorg. Chem.*, 2005, **44**, 7992.

18 T. Sajoto, P. I. Djurovich, A. B. Tamayo, J. Oxgaard, W. A. Goddard and M. E. Thompson, *J. Am. Chem. Soc.*, 2009, **131**, 9813.

19 (a) R. Tao, J. Qiao, L. Duan and Y. Qiu, *Prog. Chem.*, 2010, **22**, 2255; (b) Z. J. Liao, T. J. Zhu, B. X. Mi, Z. Q. Gao, Q. L. Fan and W. Huang, *Prog. Chem.*, 2011, **23**, 1627.

20 (a) Y. You and S. Y. Park, *Dalton Trans.*, 2009, 1267; (b) H. Fu, Y.-M. Cheng, P.-T. Chou and Y. Chi, *Mater. Today*, 2011, **14**, 472; (c) P. S. Wagenknecht and P. C. Ford, *Coord. Chem. Rev.*, 2011, **255**, 591.

21 D. Escudero, *Chem. Sci.*, 2016, **7**, 1262.

22 Q. Peng, Y. L. Niu, Q. H. Shi, X. Gao and Z. G. Shuai, *J. Chem. Theory Comput.*, 2013, **9**, 1132.

23 (a) Z. G. Shuai and Q. Peng, *Phys. Rep.*, 2014, **537**, 123; (b) Z. G. Shuai, D. Wang, Q. Peng and H. Geng, *Acc. Chem. Res.*, 2014, **47**, 3301; (c) T. Zhang, H. L. Ma, Y. L. Niu, W. Q. Li, D. Wang, Q. Peng, Z. G. Shuai and W. Z. Liang, *J. Phys. Chem. C*, 2015, **119**, 5040; (d) Q. Peng, Y. P. Yi, Z. G. Shuai and J. S. Shao, *J. Am. Chem. Soc.*, 2007, **129**, 9333.

24 I. Avilov, P. Minoofar, J. Cornil and L. De Cola, *J. Am. Chem. Soc.*, 2007, **129**, 8247.

25 B. Minaev, G. Baryshnikov and H. Ågren, *Phys. Chem. Chem. Phys.*, 2014, **16**, 1719.

26 M. J. Frisch, G. W. Trucks, H. B. Schlegel, G. E. Scuseria, M. A. Robb, J. R. Cheeseman, G. Scalmani, V. Barone, B. Mennucci, G. A. Petersson, H. Nakatsuji, M. Caricato, X. Li, H. P. Hratchian, A. F. Izmaylov, J. Bloino, G. Zheng, J. L. Sonnenberg, M. Hada, M. Ehara, K. Toyota, R. Fukuda, J. Hasegawa, M. Ishida, T. Nakajima, Y. Honda, O. Kitao, H. Nakai, T. Vreven, J. J. A. Montgomery, J. E. Peralta, F. Ogliaro, M. Bearpark, J. J. Heyd, E. Brothers, K. N. Kudin, V. N. Staroverov, R. Kobayashi, J. Normand, K. Raghavachari, A. Rendell, J. C. Burant, S. S. Iyengar, J. Tomasi, M. Cossi, N. Rega, J. M. Millam, M. Klene, J. E. Knox, J. B. Cross, V. Bakken, C. Adamo, J. Jaramillo, R. Gomperts, R. E. Stratmann, O. Yazyev, A. J. Austin, R. Cammi, C. Pomelli, J. W. Ochterski, R. L. Martin, K. Morokuma, V. G. Zakrzewski, G. A. Voth, P. Salvador, J. J. Dannenberg, S. Dapprich, A. D. Daniels, Ö. Farkas, J. B. Foresman, J. V. Ortiz, J. Cioslowski and D. J. Fox, *Gaussian09, Revision B.01*, Gaussian Inc., Wallingford CT, 2010.

27 Dalton, a molecular electronic structure program, Release Dalton 2011 (2011), see http://daltonprogram.org.

28 (a) R. Improta, UV-Visible Absorption and Emission Energies in Condensed Phase by PCM-TD-DFT Methods, in *Computational Strategies for Spectroscopy: From Small Molecules to Nanosystems*, ed. V. Barone, John Wiley & Sons, Chichester, UK, 2011, pp. 39–76; (b) G. Scalmani, M. J. Frisch, B. Mennucci, J. Tomasi, R. Cammi and V. Barone, *J. Chem. Phys.*, 2006, **124**, 094107; (c) A. D. Laurent and D. Jacquemin, *Sci. China: Chem.*, 2014, **57**, 1361.

29 Q. Peng, Y. P. Yi, J. S. Shao and Z. G. Shuai, *J. Chem. Phys.*, 2007, **126**, 114302.

30 Y. L. Niu, Q. Peng, C. M. Deng, X. Gao and Z. G. Shuai, *J. Phys. Chem. A*, 2010, **114**, 7817.

31 Z. G. Shuai, Q. Peng, H. Geng, Y. L. Niu, D. Wang, L. Y. Meng, MOMAP, a free and open-source molecular materials

This journal is © The Royal Society of Chemistry 2016

J. Mater. Chem. C, 2016, **4**, 6829–6838 | **6837**

property prediction package, Revision 0.2.004; available online: http://www.shuaigroup.net/, Beijing, China, 2014.

32 *Physics of organic semiconductor*, ed. W. Brütting and C. Adachi, Wiley-VCH, Weinheim, 2012.

33 T. Liu, B. H. Xia, Q. C. Zheng, X. Zhou, Q. J. Pan and H. X. Zhang, *J. Comput. Chem.*, 2010, **31**, 628.

34 K. Dedeian, J. M. Shi, N. Shepherd, E. Forsythe and D. C. Morton, *Inorg. Chem.*, 2005, **44**, 4445.

35 S. H. Lin, C. H. Chang, K. K. Liang, R. Chang, Y. J. Shiu, J. M. Zhang, T. S. Yang, M. Hayashi and F. C. Hsu, *Adv. Chem. Phys.*, 2002, **121**, 1.

36 (*a*) R. Englman and J. Jortner, *Mol. Phys.*, 1970, **18**, 145; (*b*) H. J. Griesser and U. P. Wild, *Chem. Phys.*, 1980, **52**, 117.

37 E. W. Schlag, S. Schneider and S. F. Fischer, *Annu. Rev. Phys. Chem.*, 1971, **22**, 465.

38 W. Siebrand, *J. Chem. Phys.*, 1967, **46**, 440.

39 H. Geng, Y. L. Niu, Q. Peng, Z. G. Shuai, V. Coropceanu and J. L. Brédas, *J. Chem. Phys.*, 2011, **135**, 104703.

40 T. Xu and S. W. Yin, *Sci. China: Chem.*, 2014, **57**, 1369.

41 Z. G. Shuai, W. J. Liu, W. Z. Liang, Q. Shi and H. Chen, *Sci. China: Chem.*, 2013, **9**, 1258.

6838 | *J. Mater. Chem. C,* 2016, **4**, 6829–6838

This journal is © The Royal Society of Chemistry 2016